# In-situ nanoscale imaging reveals self-concentrating nanomolar antimicrobial pores

Katharine Hammond, <sup>1,2,3</sup> Jonathan Moffat, <sup>4</sup> Chris Mulcahy, <sup>4</sup> Bart W Hoogenboom, <sup>2,3</sup> and

Maxim G Ryadnov<sup>1,5,\*</sup>

<sup>1</sup>National Physical Laboratory, Hampton Road, Teddington, TW11 0LW, UK
 <sup>2</sup>London Centre for Nanotechnology, University College London, London WC1H 0AH, UK
 <sup>3</sup>Department of Physics & Astronomy, University College London, London WC1E 6BT, UK
 <sup>4</sup>Oxford Instruments Asylum Research, Halifax Road, High Wycombe, HP12 3SE, UK
 <sup>5</sup>Department of Physics, King's College London, London, WC2R 2LS, UK

#### Corresponding author:

Prof Maxim G Ryadnov; National Physical Laboratory,

Hampton Road, Teddington, TW11 0LW, UK

Tel: (+44) 20 89436078; max.ryadnov@npl.co.uk

ABSTRACT: host defence peptides are critical factors of immune systems in all life forms. Considered for therapeutic development in the post-antibiotic era, these molecules rupture microbial membranes at micromolar concentrations. Here we report a self-concentrating mechanism of membrane disruption, which occurs at therapeutically more relevant nanomolar concentrations. Induced by a four-helix bacteriocin the mechanism manifests in a multi-modal disruption pattern. Using *in situ* atomic force microscopy we show that the pattern and its kinetic profiles remain the same in a range of nano-to-micromolar concentrations. We reveal that the bacteriocin creates its own boundaries in phospholipid bilayers in which it self-concentrates to promote transmembrane poration. The findings offer an exploitable insight into nanomolar antimicrobial mechanisms.

#### INTRODUCTION

Host defence mechanisms of all life forms employ antimicrobial peptides (AMPs) to determicrobial invasions. Although AMPs are evolutionarily conserved molecules, a widespread resistance against them has yet to be reported. This inspires continuous efforts to develop antimicrobial therapies on their basis. 1,2 Unlike conventional antibiotics, which must cross microbial membranes to bind to intracellular targets, AMPs attack the membranes and disrupt their lipid packing, causing cell lysis and death. 3 However, the antimicrobial action of these peptides is not limited to membrane damage. They readily engage with multiple targets in the bacterial cell (e.g. nucleic acids, ribosomes) and inhibit processes critical for cell viability (e.g. cell wall synthesis, metabolic pathways). These peptides are designed to kill microbial cells indiscriminately and rapidly, or at least within the timeframe of their proteolytic stability, i.e. minutes. To generate a substantial enough damage within this timeframe, AMPs attack in groups, which allows them to assemble into membrane-disrupting pores and lesions. The type of membrane disruption may vary from one AMP to another, and for the same peptide it may alter depending on variations in membrane composition and external stimuli. 4-6

Notwithstanding these differences, there tends to be one disruption mode per AMP within one set of environmental conditions, with each mode activated upon reaching a threshold peptide concentration in phospholipid bilayers. Such a concentration may be sufficient for pore formation, but it remains unclear how it relates to minimum inhibitory concentrations (MICs), which are used as a measure of the efficacy of antimicrobial agents. AMPs can form pores in membranes at concentrations as low as a few nanomoles per liter. Yet, these are deemed insufficient for antimicrobial activity as MICs for AMPs are typically in micromolar ranges. It is therefore argued that pores induced at nanomolar concentrations are transient, ion conducting, but do not permit molecular transport. It is further argued that antimicrobial activities correlate with the formation of stable pores, which thus far have been shown to occur at micromolar concentrations. Here we reason that stable pores can form at nanomolar concentrations, which is defined by the efficacy of an antimicrobial peptide to self-concentrate on membrane surfaces. We demonstrate this by the time-resolved imaging of pores formed by a self-concentrating mechanism permitting the same poration modes at both micro- and nanomolar concentrations.

#### RESULTS AND DISCUSSION

#### Experimental model for nanomolar antimicrobial mechanism

Demonstrating a self-concentrating mechanism and that it can support pore formation at nanomolar concentrations requires at least two capabilities: (i) an antimicrobial peptide with MICs in a sub-micromolar range, and (ii) a measurement approach allowing for direct, time-resolved visualisation at the nanoscale.

Recently, we have shown that four-helix bacteriocins, such as epidermicin NI01 and aureocin A53, disrupt membranes via a multi-modal mechanism at micromolar concentrations. Helices in these small proteins are arranged into helical hairpins, each responsible for a particular disruption mode in bacterial membranes. For example, individually hairpins of NI01 form

transmembrane lesions, circular pores, or membrane-thinning patches. However, as parts of the intact protein they act synergistically giving rise to a flower-like disruption pattern, in which the lesions with pores radially emanate from membrane thinning patches (Fig 1).<sup>11</sup>

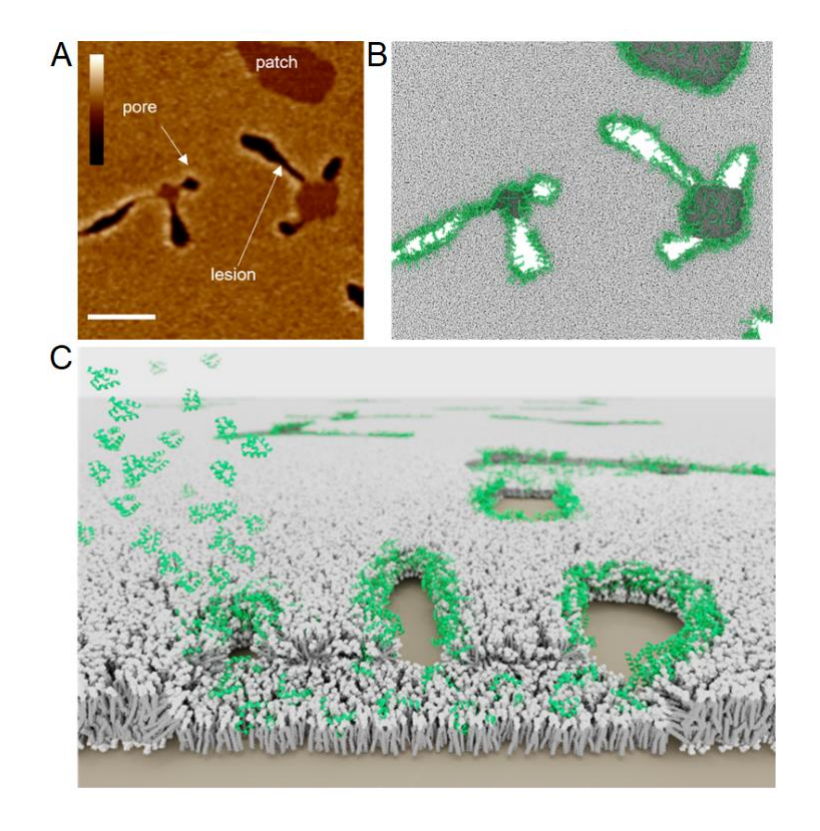


Figure 1. Flowering poration in phospholipid bilayers by epidermicin. (A) An AFM topography image of anionic POPC/POPG (3:1, molar ratio) SLBs treated with the bacteriocin (250 nM, 30 min incubation). Scale and colour bars are 200 nm and 15 nm, respectively. Reproduced under a Creative Commons license (CC BY-NC-ND 4.0) from. (B) A schematic of radially forming transmembrane lesions and pores based on the image and (C) a side-view schenatic of flowering poration in membranes caused by the bacteriocin. The schematics were drawn using a 3D computer graphics software (Blender) to illustrate the observed effects. Lipid and epidermicin molecules are shown in grey and green, respectively.

This complex mechanism, termed flowering poration, is consistent with that most AMPs adopt simpler conformations, i.e. a single  $\alpha$ -helix,  $\beta$ -sheet or hairpin, favouring one mode of membrane disruption. <sup>12,13</sup> In contrast to AMPs, the four-helix fold of NI01 can be viewed as a small ensemble of AMPs, which self-concentrate and propagate on the surface of the bacterial

membranes in a manner similar to that of pore-forming toxins, e.g. lysenin and equinatoxin. <sup>14,15</sup> As a likely consequence, NI01 more readily reaches its local threshold concentration on membranes, resulting in sub-micromolar MICs (80-330 nM) against a range of bacteria including methicillin-resistant *Staphylococcus aureus* (MRSA) and vancomycin-resistant *Enterococci* (VRE). <sup>16-18</sup> Therefore, to probe a self-concentrating mechanism and whether it can support pore formation at nanomolar concentrations we studied the impact of NI01 on phospholipid bilayers in the range of nano-to-micromolar concentrations *in situ* using atomic force microscopy (AFM). Since membrane disruption is kinetically driven and in live cells occurs over short timescales (minutes), supported lipid bilayers (SLBs) mimicking bacterial membranes were used to directly access defects formed as a result of peptide treatment. Devoid of live cell processes, such defects can be directly imaged by AFM in a time-resolved manner with a nanoscale accuracy. <sup>19</sup>

#### Imaging kinetics of membrane disruption

The kinetics of membrane disruption by NI01 were directly monitored after injecting the peptide onto the SLBs (Video S1, Fig 2A). No changes were observed over the first 50 s, which is consistent with the time during which NI01 accumulated on the membrane. It remains challenging to capture individual peptides in such a surface-bound state or S-state<sup>20</sup> in fluid membranes,<sup>21,22</sup> since peptides and lipids when imaged in liquid diffuse can rapidly across the bilayer (~ 1-2 µm²/s).<sup>23</sup> However, time-resolved AFM imaging allows monitoring nanoscale membrane defects within the relevant timescales, i.e. minutes. Indeed, in the subsequent 1.5 min, the formation of expanding membrane thinning patches became apparent (Fig 2A, B). These areas of reduced membrane thickness, by 1.5 nm, continued to grow laterally with radially expanding transmembrane lesions (Fig 2A). The lesions appeared to grow from the boundary of the patches, suggesting that a boundary edge drives membrane disruption in two stages. It starts with an intrinsic disorder of lipids, which offers less resistance to pore

formation, and introduces the unfavourable line tension of the boundary accelerating peptide binding.<sup>24</sup>

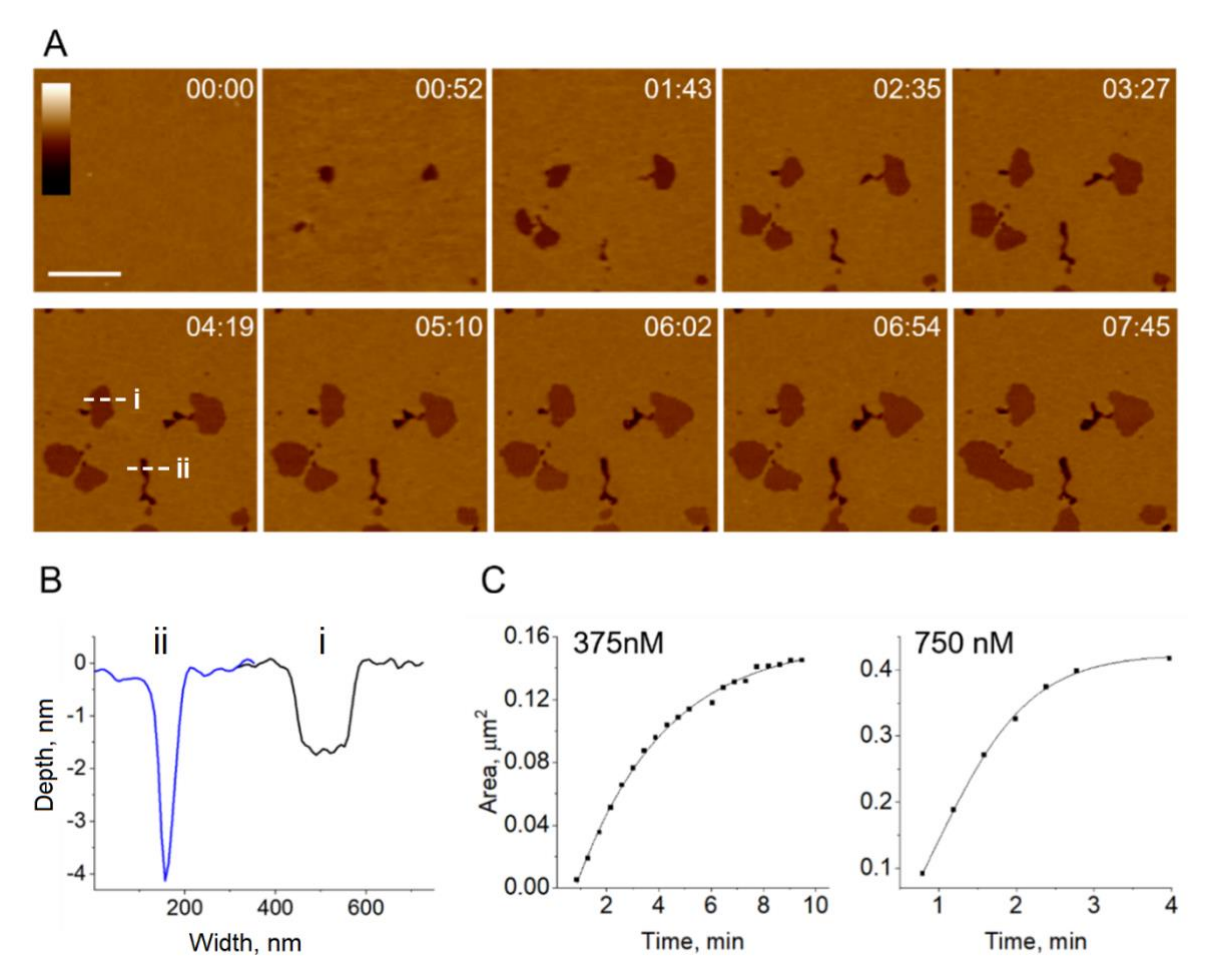


Figure 2. Time-resolved imaging of reconstituted membranes treated with NI01. (A) AFM topography images of anionic SLBs (see Methods and Materials) treated with NI01 at a concentration of 375 nM (in a ~200  $\mu$ L volume). Images are digital zooms of selected frames from continuous imaging (Video S1) showing the initial formation of defects in the membrane. Time stamps are referenced to the moment of injection (00:00) of NI01 into the tubing, which then travels to the fluid cell. Patches of membrane thinning form first, with transmembrane lesions and pores growing from the boundary edge of the patches. Colour (height) and scale bars are 15 nm and 500 nm, respectively. (B) Cross-section line profiles along the white dashed lines in (A) at time 04:19, showing the depth of membrane thinning patches (i) and transmembrane lesions (ii). (C) Total defect area plotted versus time for all frames in the first 10 min of imaging at 375 nM peptide (left) and in the first 5 min of imaging at 750 nM peptide (right).

Compared with pore-forming proteins such as lysenin and equinatoxin, <sup>25,26</sup> which prefer to porate membranes on existing boundaries between phase-separated lipid domains, NI01 then creates its own, new domain boundaries between thinned and unaffected membrane areas. The new formed boundaries become preferred locations for further peptide recruitment, which drives flowering poration to completion. As peptide supply is depleted in the fluid cell of the microscope, the rate of defect formation decreases reaching a saturation point (Fig 2C). However, the morphological characteristics of the defects and their sequential formation, i.e. from membrane thinning via transmembrane poration to the saturation of defect growth, remain independent of the concentration used. Indeed, the same behaviour and comparable kinetic profiles were observed at double the peptide concentration used (Fig 2C, Video S2, Fig S2). The higher concentration only led to larger total defect areas which grew at double the rate observed for the lower peptide concentration.

The kinetic profiles observed are different from those characteristic of pore expansion mechanisms resulting in complete membrane disintegration, <sup>21,27-29</sup> and from those supporting different modes of membrane disruption at different peptide concentrations. <sup>30-32</sup> All these cases are concentration dependent and promote the non-specific, progressive disruption of the phospholipid bilayer, which is proportional to the amount of peptide available on the membrane surface. In contrast, NI01 creates the same membrane disruption pattern at any concentration used within the nano-to-micromolar range and within the same timeframe, suggesting that its local threshold concentration does not depend on the concentration used either. Therefore, once the threshold is reached, which manifests in the completed disruption pattern, the kinetics of membrane disruption should remain the same. To test this conjecture, we added three subsequent injections of NI01 to the SLBs with fully formed floral patterns. The total defect area first decreased and then resumed growth exhibiting kinetics, which matched those of the first injections (Fig 3A).

The initial decrease occurred at the expense of membrane thinning patches: the areas of the patches shrunk, whereas their boundaries elongated, initiating the growth of new transmembrane lesions (see transitions from left to middle, and middle to right column in Fig 3B, C). No noticeable changes occurred in the transmembrane lesions which were formed during the previous injections and no new areas of membrane thinning could be observed.

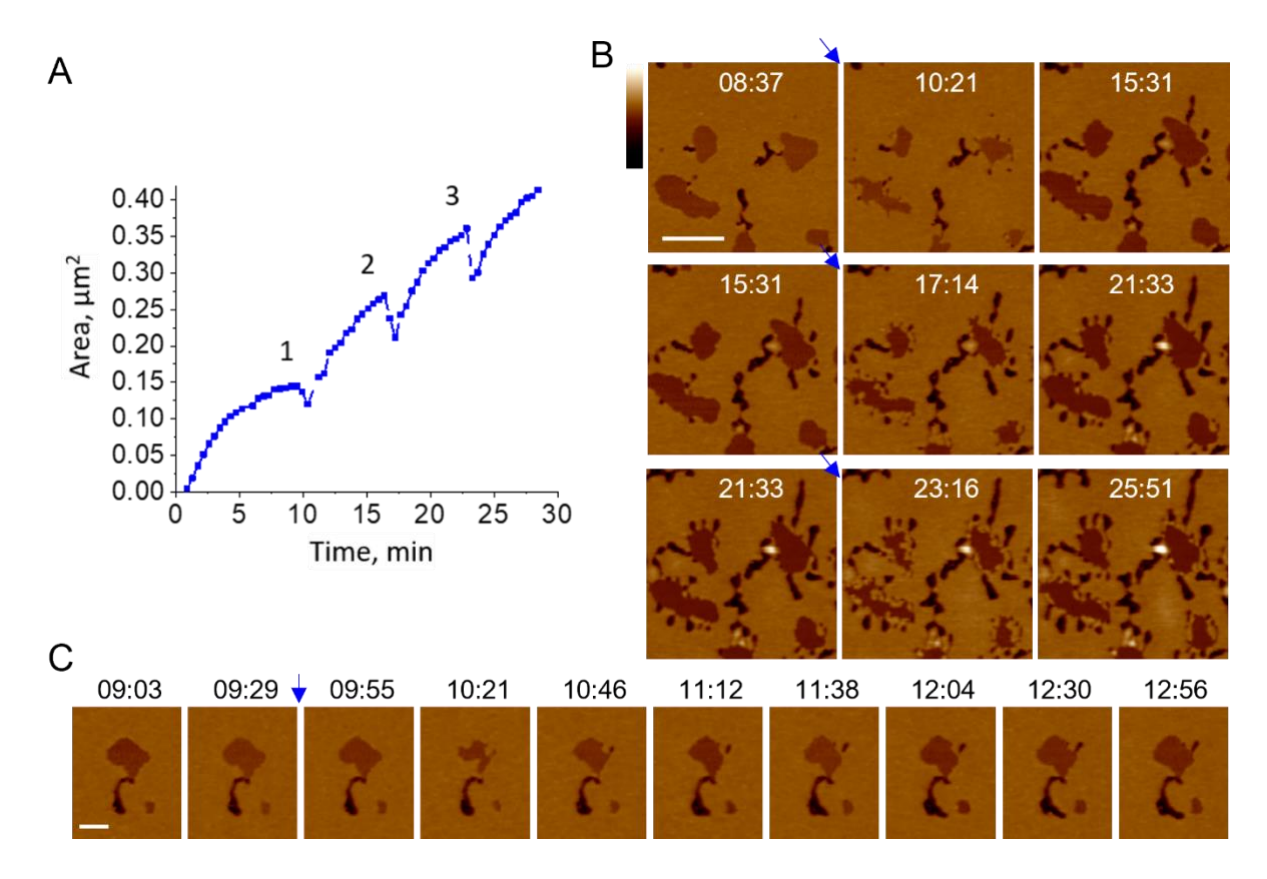


Figure 3. Repeated injections of NI01 onto membranes. (A) A plot of total defect coverage versus time (min) for anionic SLBs treated with NI01 (375 nM). The results for the first ~10 min are duplicated from Figure 2C. Three additional peptide injections are applied over 30 min (labelled 1-3) and each peptide injection restarts the growth of the defects followed by the same kinetics trait. (B) Digital zoom of selected frames from Video S1 showing the response of a single area of membrane to three additional injections (top, middle and bottom rows, respectively). Blue arrows highlight injection points. Thinned membrane patches shrink and elongate their boundaries, new channels are formed at the boundary edge, and existing lesions do not respond to the injections. (C) A digital zoom of selected frames from Video

S1 showing the response of a single defect to the injection of additional peptide (highlighted by blue arrow). Colour bars are 15 nm in all images, scale bars are 500 nm (B) and 200 nm (C).

These results confirm that once formed membrane thinning patches act as recruitment sites for additional peptide from which it proceeds forming new transmembrane lesions.

Quantitative analyses of defect areas revealed that thinned membrane patches decreased in area by 50% after peptide injection (Fig S3A, E). This drop in thinned membrane area was accompanied by an increase in boundary length per unit area of 100% for the thinned membrane patches (Fig S3A, E). This effect was specific for the thinned membrane patches. No such response to peptide injection was found for the transmembrane lesions (Fig S3B). Over time, the transmembrane lesions grew in size, but their boundary lengths per unit area remained approximately constant (Fig S3B). An apparent lower propensity of the lesions to recruit more peptide could be attributed to a lower line tension at the lesion edge. Plotting the absolute values of the boundary length per unit area for the defects showed that the transmembrane lesions have a more elongated boundary than the thinned membrane patches, which is consistent with a lower line tension (Fig S3C).

The initial decrease of the thinned membrane domains indicates that additional peptide preferentially accumulates at the domain boundaries. From the subsequent transmembrane poration at these boundaries, we conclude that the accumulation and thereby enhanced local concentration of NI01 facilitates the formation of transmembrane defects at the boundaries. The changes in the boundary shape also indicate that the boundary of thinned membrane patches undergoes significant remodelling, which is consistent with peptide binding to the edge, reducing the line tension, and allowing a more elongated boundary edge. The simultaneous formation of new transmembrane defects at the remodelled boundary provides the confirmation of a local peptide concentration that is sufficient to surpass the threshold required for poration.

#### Forming pores at low nanomolar concentrations

Since no differences were observed in the mode of membrane disruption by NI01 as a function of concentration, the peptide should induce the same defect patterns on membranes at a lower range of nanomolar concentrations within the same timeframe. This is in contrast to AMPs, which at such low concentrations do not disrupt membranes.

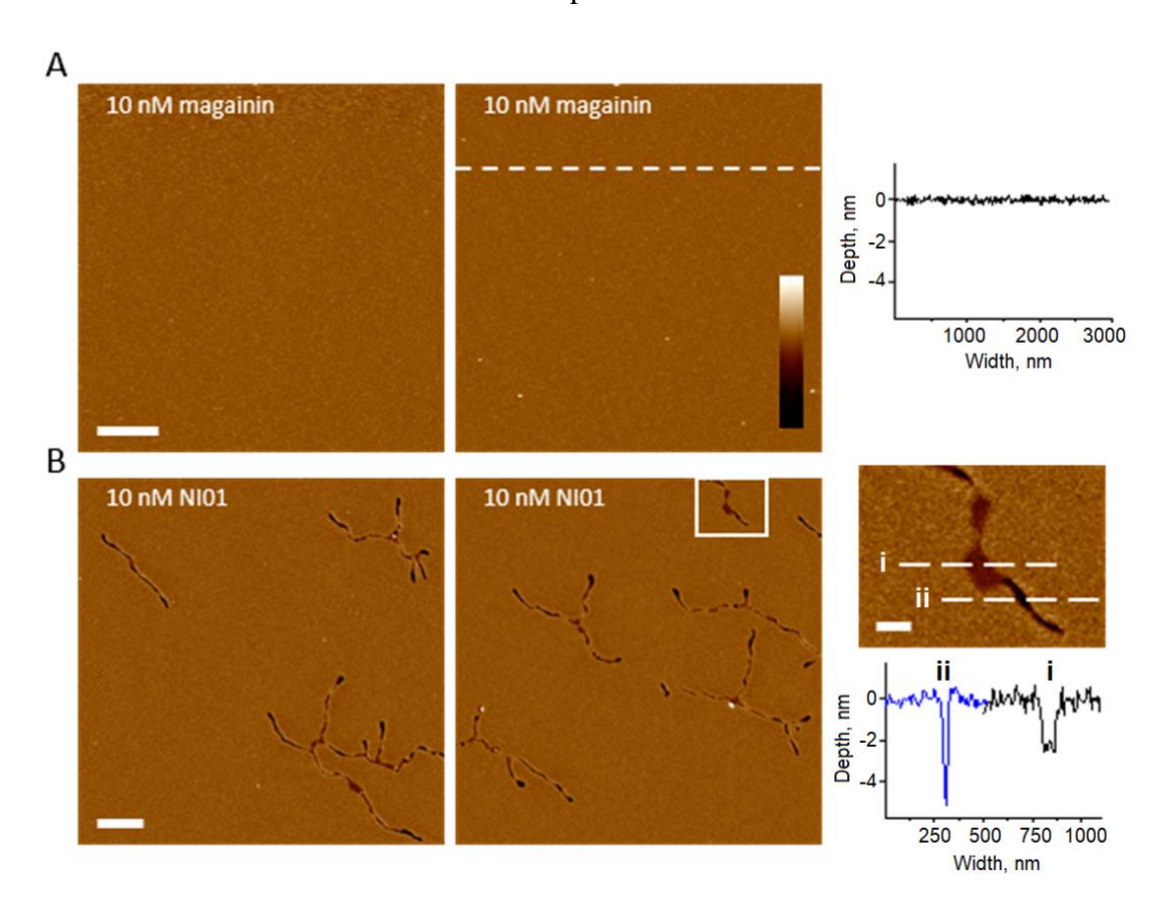


Figure 4. Comparison of NI01 to magainin 2 at nanomolar concentrations. Representative topography images of POPC/POPG (3:1, molar ratio) SLBs after 30 min of incubation with (A) magainin 2 (10 nM) and (B) NI01 (10 nM). For each case, cross-section line profiles along the dotted lines are shown, to indicate depth profiles of the membrane surfaces. Two different SLB areas of the same sample are shown for each case. A digital zoom of the white box in (B) highlights membrane thinning patches (i) and transmembrane lesions (ii). Colour (height) and scale bars are 15 nm and 500 nm, respectively. The scale bar for the zoom image is 100 nm.

To probe this, membrane disruption by NI01 was compared with that by magainin 2, an archetypal AMP known to induce transmembrane pores in SLBs at micromolar concentrations

(Fig S4).<sup>32</sup> As expected, no changes were observed in SLBs treated with magainin 2 at nanomolar concentrations (10 nM): after 30 min of incubation, the surface of the SLB remained featureless (Fig 4A). In contrast, NI01 produced its characteristic floral pattern in SLBs at these concentrations. Over 30-min incubations, the surface of the SLB showed transmembrane lesions growing from thinned membrane patches (Fig 4B). The findings confirm that upon the formation of the thinned membrane areas NI01 self-concentrates at their boundaries reaching its threshold concentration to form transmembrane lesions. The smaller patch areas observed at these low nanomolar concentrations are consistent with that larger areas are produced at higher concentrations (Fig 2), and indicate that transmembrane lesions start forming as soon as the boundaries of the patches become apparent and able to recruit all the peptide available to complete the disruption pattern. Instead of accumulating in and expanding the patch areas, NI01 self-concentrates at available boundaries forming transmembrane defects and completing the pattern.

#### **CONCLUSION**

These findings prompt a working model for the self-concentrating effect by NI01, drawing parallels with the mechanisms of pore-forming peptides, proteins, and toxins. Similar to AMPs, NI01 binds to and accumulates on the membrane surfaces to form initial defects, i.e. membrane thinning patches. This occurs during a lag-time phase typical for most AMPs following the S-state,<sup>33</sup> which allows time for a transition into folded forms and oligomerisation at the membrane surface until threshold concentrations for defect formation are reached. Once started forming, thinned membrane patches create boundary edges, which due to their inherent disorder and high line tension actively recruit more NI01. The bacteriocin molecules recruited from solution on to the membranes are likely to undergo a structural transformation. In solution, NI01 exits as a monomer folded as a globular four-helix bundle, with the hydrophobic residues forming the core of the bundle to stabilise the fold.<sup>11</sup> In the membrane the core is no

longer needed and can no longer support the fold given competing interactions with phospholipids. Therefore, the bacteriocin re-folds with its constituent helices re-arranging to better integrate in the membrane. Because at the boundary edges lipids are more distorted and their hydrophobic, aliphatic chains are more exposed to NI01, the helices re-orient their hydrophobic faces to engage with the lipids prompting the remodelling of the boundary. Thus, membrane thinning continues with increasing local concentrations until it reaches a concentration threshold, at which the boundary starts remodelling and lesions are formed. This scenario is accompanied by oligomerisation in a manner similar to that of four-helix toxins assembling into multimers which porate membranes.<sup>34</sup> This is consistent with the preference of transmembrane pores to form at thinned boundary edges and is akin to the way some poreforming proteins exploit phase-separated lipid domains. 25,26 However, NIO1 arranges and regulates forming boundaries by self-concentrating, which allows it to complete its disruption pattern at low nanomolar concentrations. The multimodal mechanism of NI01 progresses by recruiting peptide through membrane thinning domains, which grow rapidly reaching poration thresholds at the domain boundaries, even at low nanomolar concentrations, driving the pore formation to completion.

#### MATERIALS AND METHODS

#### **Peptide Synthesis and Purification**

NI01 was assembled in a Liberty microwave peptide synthesizer (CEM Corporation) using conventional Fmoc/tBu synthesis protocols and HBTU/DIPEA coupling reagents, at 0.1 mmol scale, on a Fmoc-Ala-Wang resin. The bacteriocin was capped at its N-terminus using p-nitrophenylformate, then was cleaved and deprotected using a cleavage cocktail (94% TFA, 2% TIS, 2% DODT, 2% water), then purified by semi-preparative RP-HPLC. The purity and identity of NI01 was confirmed by analytical RP-HPLC (≥95%) and MALDI-ToF mass-spectrometry: MS [M + H]<sup>+</sup>: m/z 6072.3 (calc.), 6072.8 (found). Analytical and semi-

preparative RP-HPLC runs were performed on a Thermo Scientific Dionex HPLC System (Ultimate 3000) using a Vydac C18 analytical and semi-preparative (both 5 μm) columns. Analytical runs used a 10-70% B gradient over 30 min at 1 mL/min, semi-preparative runs were optimised for the peptide, at 4.5 mL/min. Detection was at 280 and 214 nm. Buffer A and buffer B were 5% and 95% (v/v) aqueous CH<sub>3</sub>CN containing 0.1% TFA.

#### **Lipid Vesicle Preparation**

1-palmitoyl-2-oleoyl-glycero-3-phosphocholine (POPC) with 1-palmitoyl-2-oleoyl-sn-glycero-3-phospho-(1'-rac-glycerol) (POPG) lipids were used to assemble liposomes in 3:1, molar ratios. The lipids were purchased from Avanti Polar Lipids (Alabaster, USA). The lipids were weighted up and were dissolved in chloroform. The preparations were then dried under a nitrogen stream to form a thin film, and the film was hydrated in 10 mM phosphate buffer (pH 7.4), vortexed for 2 min and bath sonicated for 30 min. The obtained suspension was extruded using a hand-held extruder (Avanti Polar lipids) (29 times, polycarbonate filter, 0.05  $\mu$ m) to give a clear solution of small unilamellar vesicles following the re-suspension of vesicles to a final concentration of 1 mg/mL.

#### **Preparation of SLBs for In-Liquid AFM Imaging**

SLBs were formed using a vesicle fusion method as described elsewhere.<sup>35</sup> Briefly, freshly prepared POPC/POPG (3:1, molar ratio) vesicles (5 µL 1 mg/mL) were added to cleaved mica that was pre-hydrated in 20 mM MOPS, 120 mM NaCl, 20 mM MgCl<sub>2</sub> (pH 7.4). After incubation over 45 min, the samples were washed 10 times with an imaging buffer (20 mM MOPS, with 120 mM NaCl, pH 7.4) to remove unfused vesicles. AFM was used to confirm that the resulting SLBs were free of defects and were flat to within < 0.3 nm before use in experiments. Mica discs (Agar Scientific, Stansted, UK) were glued to a metal puck, and freshly cleaved prior to lipid deposition.

#### **Peptide Addition to the SLBs**

All peptide solutions were prepared in AFM imaging buffer to avoid introducing changes in the ionic strength or pH of the solutions. Peptide solutions were then injected directly into the fluid cell via a syringe and tubing system. Tubes were pre-filled with the AFM imaging buffer to prevent the introduction of air bubbles. The fluid cell has a volume of c.100  $\mu$ L and each injection consisted of c. 200  $\mu$ L peptide solution. Therefore, the imaging solution in the fluid cell is entirely replaced with the injected solution and the concentration of the peptide solution was prepared at the final desired concentration, whereas the excess above the 100  $\mu$ L capacity of the fluid cell is flushed out into a waste syringe.

#### Photothermal Actuation and In-Situ Injection Set-Up

The AFM experiments were carried out with a Cypher ES AFM (Oxford Instruments Asylum Research) equipped with photothermal actuation (blueDrive<sup>TM</sup>). This AFM has a fully sealed measurement cell that allows the perfusion of liquids and gases during measurements (Fig S1). The peptide solution is introduced during imaging to capture dynamics in real time. The introduction of a new liquid into the cell can destabilise the mechanical driving mechanism commonly found in conventional AFM systems and often measurements have to be stopped to retune the probe. This is due to changes in the environmental conditions, namely the size and concentration of the liquid droplet and the operating temperature. Photothermal excitation of the cantilever was employed as it can be less sensitive to these changes. This involves direct actuation with a secondary laser with a wavelength of 405 nm. This laser is directed to the base of the cantilever and modulation of the power causes the probe to oscillate due to the photothermal effect. Small changes in temperature cause the probe to bend at the base of the cantilever whilst there are negligible differences at the tip. Time-resolved imaging was performed using the actuation laser at a low power (0.3 mW DC) to avoid artefacts due to sample heating.

#### **AFM Operation**

Images were recorded in amplitude modulation (tapping, AC) AFM mode, using photothermal excitation, with an Olympus AC10 probe (nominal resonance frequency in air = 1500 kHz; nominal spring constant = 0.1 N/m, tip radius < 10 nm, tip side angle =  $10 ^{\circ}$ ). In solution, the cantilever was actuated at its in-liquid resonance frequency of 443 kHz to an amplitude of ~0.5 nm. Images were recorded with a setpoint amplitude at approximately 60 % of the free amplitude just above the surface, with the setpoint and gains continuously adjusted to obtain the lowest imaging force without sacrificing contrast and resolution. Images were recorded at line rates of 20 Hz, resulting in frame times of ~25 seconds.

#### **Post-Image Processing**

All image processing was done using Gwyddion (http://gwyddion.net/). Background tilt across the image was removed via plane-fitting and first-order line fitting. Following plane fitting and first-order levelling, the height at the membrane surface was defined as 0 nm to allow comparison between all images. All depth profiles were plotted using Origin (OriginLab Corporation).

#### SUPPORTING INFORMATION

Figures and Movies are included as described in the text: experimental in situ injection set-up for AFM operation, AFM images and videos with quantitative analyses.

#### **NOTES**

The authors declare no competing financial interests.

#### **ACKNOWLEDGEMENTS**

We acknowledge funding from the UK's Department for Business, Energy and Industrial Strategy and Innovate UK (grant: 103358). We thank Dr Adrian Hodel for his help with the model of pore formation and Dr Andrew Yacoot for his advice on the content of the work.

#### REFERENCES

- (1) Kosikowska, P.; Lesner, A. Antimicrobial Peptides (AMPs) as Drug Candidates: A Patent Review (2003–2015). *Expert Opin. Ther. Pat.* **2016**, *26* (6), 689–702.
- (2) Mookherjee, N.; Anderson, M. A.; Haagsman, H. P.; Davidson, D. J. Antimicrobial Host Defence Peptides: Functions and Clinical Potential. *Nat. Rev. Drug Discov.* 2020, 19 (5), 311–332.
- (3) Nguyen, L. T.; Haney, E. F.; Vogel, H. J. The Expanding Scope of Antimicrobial Peptide Structures and Their Modes of Action. *Trends Biotechnol.* **2011**, 29 (9), 464–472.
- (4) Guha, S.; Ghimire, J.; Wu, E.; Wimley, W. C. Mechanistic Landscape of Membrane-Permeabilizing Peptides. *Chem. Rev.* **2019**, *119* (9), 6040–6085.
- (5) Sani, M.-A.; Separovic, F. How Membrane-Active Peptides Get into Lipid Membranes. *Acc. Chem. Res.* **2016**, *49* (6), 1130–1138.
- (6) Li, J.; Koh, J.-J.; Liu, S.; Lakshminarayanan, R.; Verma, C. S.; Beuerman, R. W. Membrane Active Antimicrobial Peptides: Translating Mechanistic Insights to Design. Front. Neurosci. 2017, 11, 73.
- (7) Lee MT, Sun TL, Hung WC, Huang HW.
  Process of inducing pores in membranes by melittin. Proc Natl Acad Sci U S A. 2013,
  110, 14243-14248.
- (8) Hanke W, Methfessel C, Wilmsen HU, Katz E, Jung G, Boheim G. Melittin and a chemically modified trichotoxin form alamethicin-type multi-state pores. *Biochim Biophys Acta*. 1983, 727, 108-114.
- (9) Last NB, Miranker AD. Common mechanism unites membrane poration by amyloid and antimicrobial peptides. *Proc Natl Acad Sci U S A*. 2013, 110, 6382-6387.
- (10) Yang L, Weiss TM, Lehrer RI, Huang HW. Crystallization of antimicrobial pores in membranes: magainin and protegrin. *Biophys J*, 2000, 79, 2002-2009.
- (11) Hammond, K.; Lewis, H.; Halliwell, S.; Desriac, F.; Nardone, B.; Ravi, J.;

- Hoogenboom, B. W.; Upton, M.; Derrick, J. P.; Ryadnov, M. G. Flowering Poration—A Synergistic Multi-Mode Antibacterial Mechanism by a Bacteriocin Fold. *iScience* **2020**, *23* (8), 101423.
- (12) Juretić, D.; Vukičević, D.; Tossi, A. Tools for Designing Amphipathic Helical Antimicrobial Peptides. In *Methods in Molecular Biology Vol 1548*; Hansen, P., Ed.; Humana Press: New York, NY, 2017; pp 23–34.
- (13) Wang, G.; Li, X.; Wang, Z. APD3: The Antimicrobial Peptide Database as a Tool for Research and Education. *Nucleic Acids Res.* **2016**, *44* (D1), D1087–D1093.
- (14) Bokori-Brown M, Martin TG, Naylor CE, Basak AK, Titball RW, Savva CG. Cryo-EM structure of lysenin pore elucidates membrane insertion by an aerolysin family protein.

  Nat Commun. 2016, 7, 11293.
- (15) Barlič, A.; Gutiérrez-Aguirre, I.; Caaveiro, J. M. M.; Cruz, A.; Ruiz-Argüello, M.-B.; Pérez-Gil, J.; González-Mañas, J. M. Lipid Phase Coexistence Favors Membrane Insertion of Equinatoxin-II, a Pore-Forming Toxin from Actinia Equina. *J. Biol. Chem.* 2004, 279 (33), 34209–34216.
- (16) Sandiford, S.; Upton, M. Identification, Characterization, and Recombinant Expression of Epidermicin NI01, a Novel Unmodified Bacteriocin Produced by Staphylococcus Epidermidis That Displays Potent Activity against Staphylococci. *Antimicrob. Agents Chemother.* **2012**, *56* (3), 1539–1547.
- (17) Gibreel, T. M.; Upton, M. Synthetic Epidermicin NI01 Can Protect Galleria Mellonella Larvae from Infection with Staphylococcus Aureus. *J. Antimicrob. Chemother.* 2013, 68 (10), 2269–2273.
- (18) Halliwell, S.; Warn, P.; Sattar, A.; Derrick, J. P.; Upton, M. A Single Dose of Epidermicin NI01 Is Sufficient to Eradicate MRSA from the Nares of Cotton Rats. *J. Antimicrob. Chemother.* **2017**, 72 (3), 778–781.

- (19) Hammond, K.; Ryadnov, M. G.; Hoogenboom, B. W. Atomic Force Microscopy to Elucidate How Peptides Disrupt Membranes. *Biochim. Biophys. Acta Biomembr.* **2021**, *1863* (1), 183447.
- (20) Huang, H. W. Action of Antimicrobial Peptides: Two-state model. *Biochemistry*, **2000**, 39 (29), 8347-8352.
- (21) Rakowska, P. D.; Jiang, H.; Ray, S.; Pyne, A.; Lamarre, B.; Carr, M.; Judge, P. J.; Ravi, J.; Gerling, U. I. M.; Koksch, B.; Martyna, G. J.; Hoogenboom, B. W.; Watts, A.; Crain, J.; Grovenor, C. R. M.; Ryadnov, M. G. Nanoscale Imaging Reveals Laterally Expanding Antimicrobial Pores in Lipid Bilayers. *Proc. Natl. Acad. Sci.* 2013, *110* (22), 8918–8923.
- (22) Dufrêne, Y. F.; Ando, T.; Garcia, R.; Alsteens, D.; Martinez-Martin, D.; Engel, A.; Gerber, C.; Müller, D. J. Imaging Modes of Atomic Force Microscopy for Application in Molecular and Cell Biology. *Nat. Nanotechnol.* **2017**, *12* (4), 295–307.
- (23) Guo, L.; Har, J. Y.; Sankaran, J.; Hong, Y.; Kannan, B.; Wohland, T. Molecular Diffusion Measurement in Lipid Bilayers over Wide Concentration Ranges: A Comparative Study. *ChemPhysChem* **2008**, *9* (5), 721–728.
- (24) Labuda, A.; Hohlbauch, S.; Kocun, M.; Limpoco, F. T.; Kirchhofer, N.; Ohler, B.; Hurley, D. Tapping Mode AFM Imaging in Liquids with BlueDrive Photothermal Excitation. *Micros. Today* **2018**, *26* (6), 12–17.
- (25) Barlič, A.; Gutiérrez-Aguirre, I.; Caaveiro, J. M. M.; Cruz, A.; Ruiz-Argüello, M.-B.; Pérez-Gil, J.; González-Mañas, J. M. Lipid Phase Coexistence Favors Membrane Insertion of Equinatoxin-II, a Pore-Forming Toxin from Actinia Equina. *J. Biol. Chem.* 2004, 279 (33), 34209–34216.
- (26) Schön, P.; García-Sáez, A. J.; Malovrh, P.; Bacia, K.; Anderluh, G.; Schwille, P. Equinatoxin II Permeabilizing Activity Depends on the Presence of Sphingomyelin and

- Lipid Phase Coexistence. Biophys. J. 2008, 95 (2), 691–698.
- (27) Henderson, J. M.; Waring, A. J.; Separovic, F.; Lee, K. Y. C. Antimicrobial Peptides Share a Common Interaction Driven by Membrane Line Tension Reduction. *Biophys. J.* **2016**, *111* (10), 2176–2189.
- (28) De Santis, E.; Alkassem, H.; Lamarre, B.; Faruqui, N.; Bella, A.; Noble, J. E.; Micale, N.; Ray, S.; Burns, J. R.; Yon, A. R.; Hoogenboom, B. W.; Ryadnov, M. G. Antimicrobial Peptide Capsids of de Novo Design. *Nat. Commun.* **2017**, *8* (1), 2263.
- (29) Pan, J.; Khadka, N. K. Kinetic Defects Induced by Melittin in Model Lipid Membranes: A Solution Atomic Force Microscopy Study. *J. Phys. Chem. B* **2016**, *120* (20), 4625–4634.
- (30) Heath, G. R.; Harrison, P. L.; Strong, P. N.; Evans, S. D.; Miller, K. Visualization of Diffusion Limited Antimicrobial Peptide Attack on Supported Lipid Membranes. *Soft Matter* **2018**, *14* (29), 6146–6154.
- (31) Lam, K. L. H.; Wang, H.; Siaw, T. A.; Chapman, M. R.; Waring, A. J.; Kindt, J. T.; Lee, K. Y. C. Mechanism of Structural Transformations Induced by Antimicrobial Peptides in Lipid Membranes. *Biochim. Biophys. Acta Biomembr.* 2012, 1818 (2), 194–204.
- (32) Hammond, K.; Lewis, H.; Faruqui, N.; Russell, C.; Hoogenboom, B. W.; Ryadnov, M. G. Helminth Defense Molecules as Design Templates for Membrane Active Antibiotics.
  ACS Infect. Dis. 2019, 5 (8), 1471–1479.
- (33) Haney, E. F.; Mansour, S. C.; Hancock, R. E. W. Antimicrobial Peptides: An Introduction. *Methods Mol Biol.* **2017**, *1548*, 3–22.
- (34) Michalek, M.; Sönnichsen, F. D.; Wechselberger, R.; Dingley, A. J.; Hung, C. W.; Kopp, A.; Wienk, H.; Simanski, M.; Herbst, R.; Lorenzen, I. et al. Structure and function of a unique pore-forming protein from a pathogenic acanthamoeba. *Nat. Chem. Biol.* 2013, 9, 37-42.

(35) Lin, W.-C.; Blanchette, C. D.; Ratto, T. V.; Longo, M. L. Lipid asymmetry in DLPC/DSPC-supported lipid bilayers: a combined AFM and fluorescence microscopy study. *Biophys. J*, **2006**, *90*, 228-237.

### **Supporting Information**

## In-situ nanoscale imaging reveals self-concentrating nanomolar antimicrobial pores

Katharine Hammond, Jonathan Moffat, Chris Mulcahy, Bart W Hoogenboom and Maxim G Ryadnov

#### **Figures and Videos**

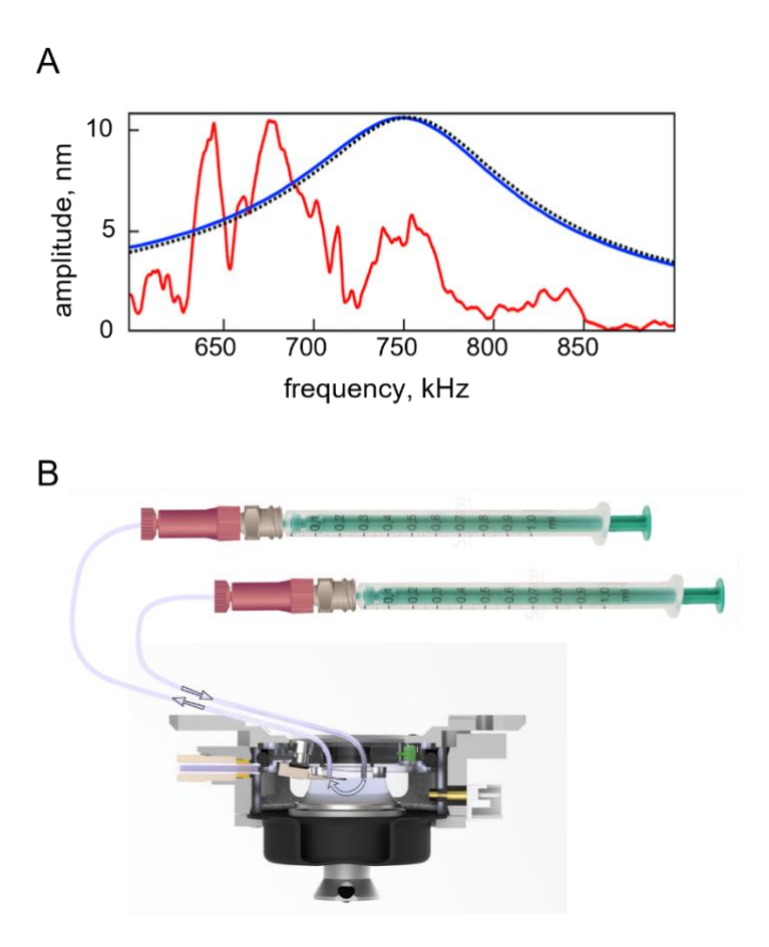
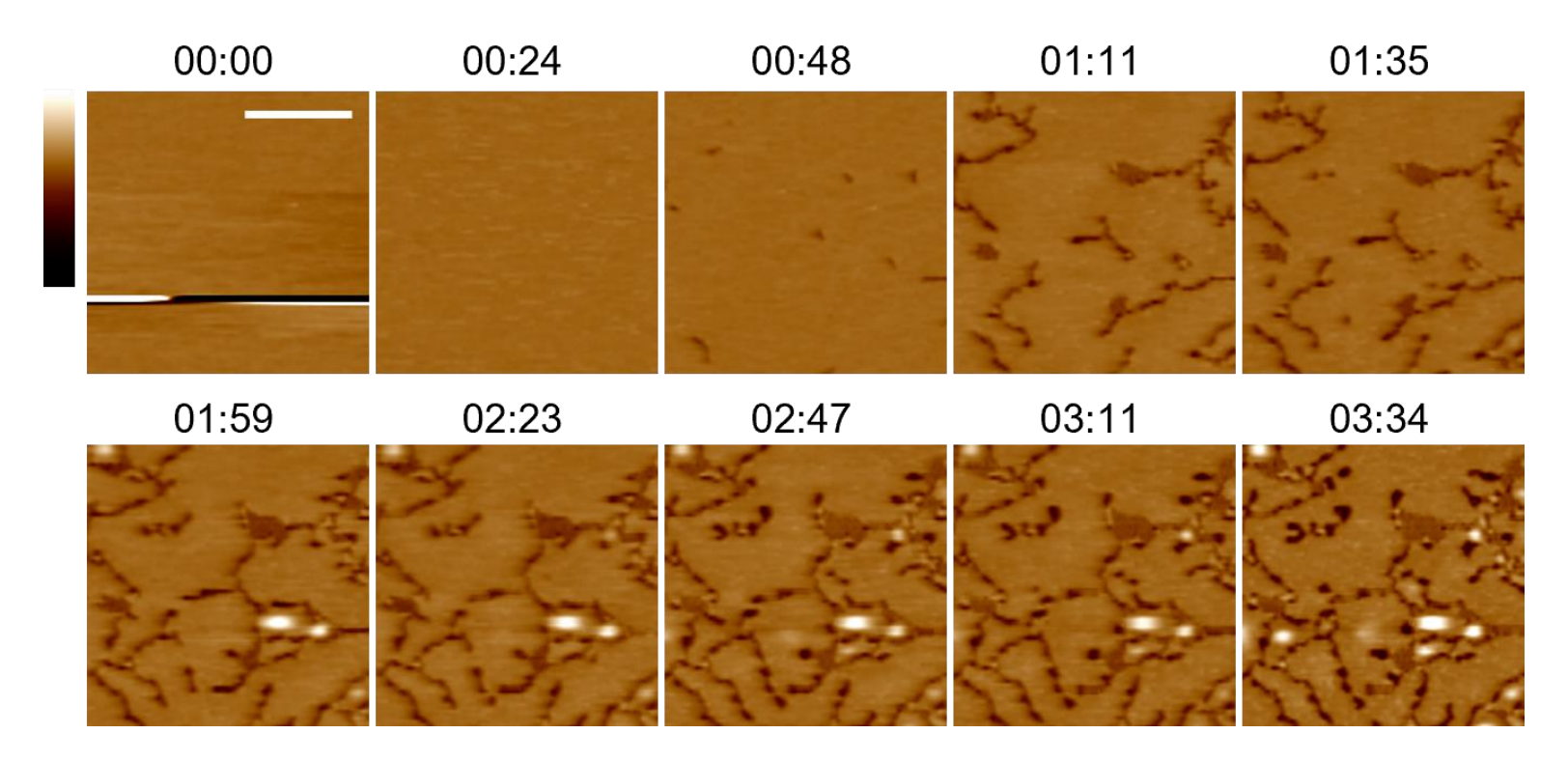


Figure S1. Set up of Cypher ES AFM (Oxford Instruments Asylum Research) equipped with photothermal actuation (blueDrive<sup>TM</sup>). (A) Comparison of cantilever response (amplitude vs frequency) for piezoelectric cantilever excitation (red) and photothermal excitation (blue). Piezoelectric excitation subjects the entire fluid cell to mechanical excitation resulting in multiple peaks. Photothermal methods directly excite the cantilever, resulting in a single peak. Spectra taken in water, reproduced with permission from<sup>24</sup>. (B) Schematic cut away of the sealed measurement cell of the AFM showing connection of tubing to allow the introduction and withdrawal of liquid.



**Figure S2. Time-resolved imaging of membrane disruption by NI01.** (A) Representative AFM topography images of anionic POPC/POPG (3:1, molar ratio) SLBs following injection of NI01 (750 nM) at 00:00 min. The images are digital zooms of selected frames from Video S2. Scale and colour (height) bars are 500 nm and 15 nm, respectively.

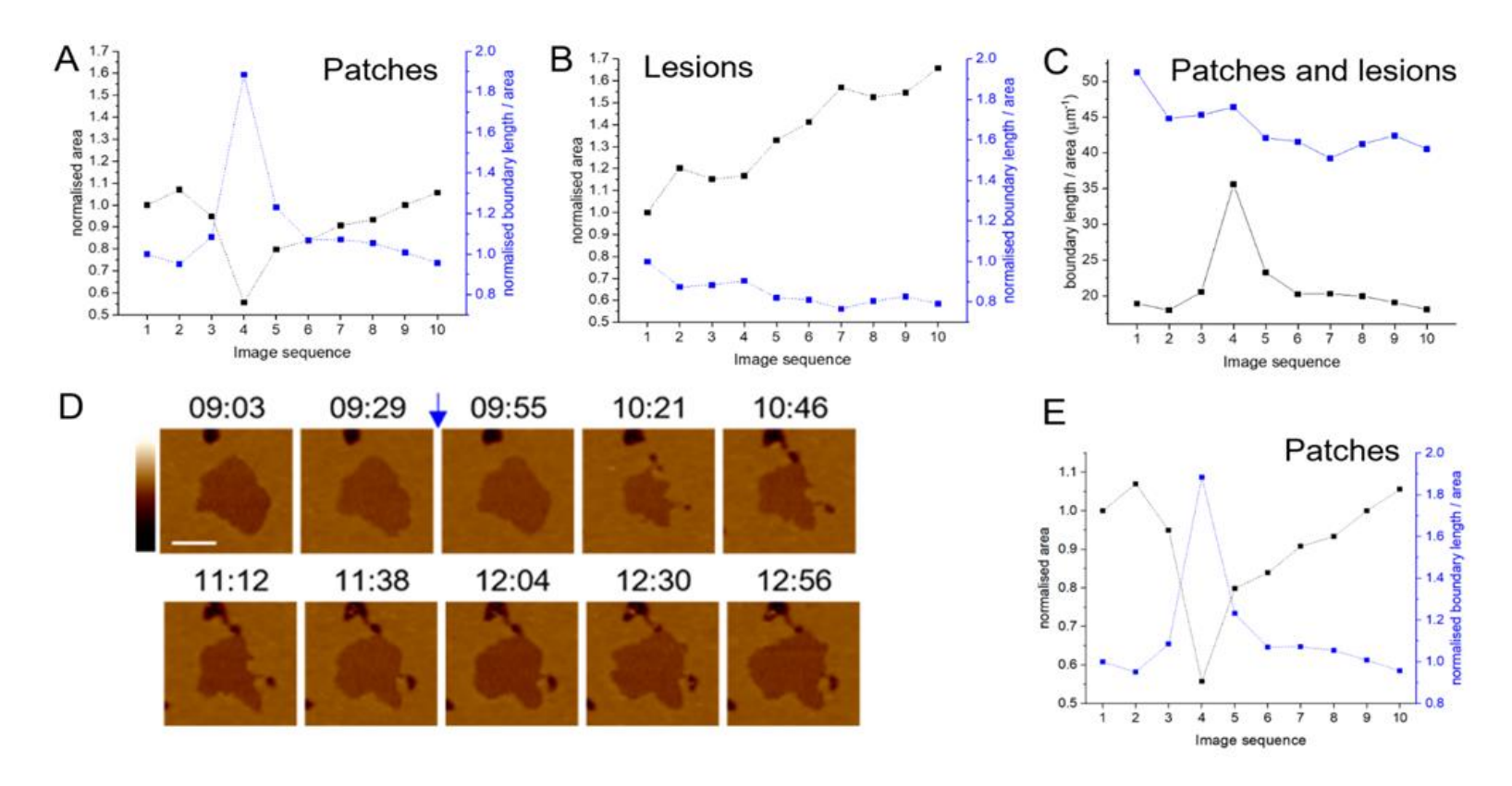


Figure S3. Response of membrane thinning patches to additional injections of NI01. (A, B) Plots of the surface area (black) and boundary length per unit area (blue) for the thinned membrane patches (A) from topography images in Fig 3C. Image sequence numbers refer to the topography images labelled from left to right, and the point of injection occurs after image 2, as highlighted by the blue arrow. Values are normalised to the value in image 1. (C) Comparison of the absolute value for boundary length per unit area between transmembrane channels (blue) and patches (black) in Fig 3C. (D -E) topography images (D) and corresponding plots of the surface area (black) and boundary length per unit area (blue) for a thinned membrane patch (E). Image sequence numbers refer to the topography images in (D), labelled from left to right and the point of injection is highlighted by the blue arrow. Values are normalised to the value in image 1. Images in (D) are digital zooms of selected frames from continuous imaging (Video S1). Colour (height) and scale bars are 15 nm and 180 nm, respectively.

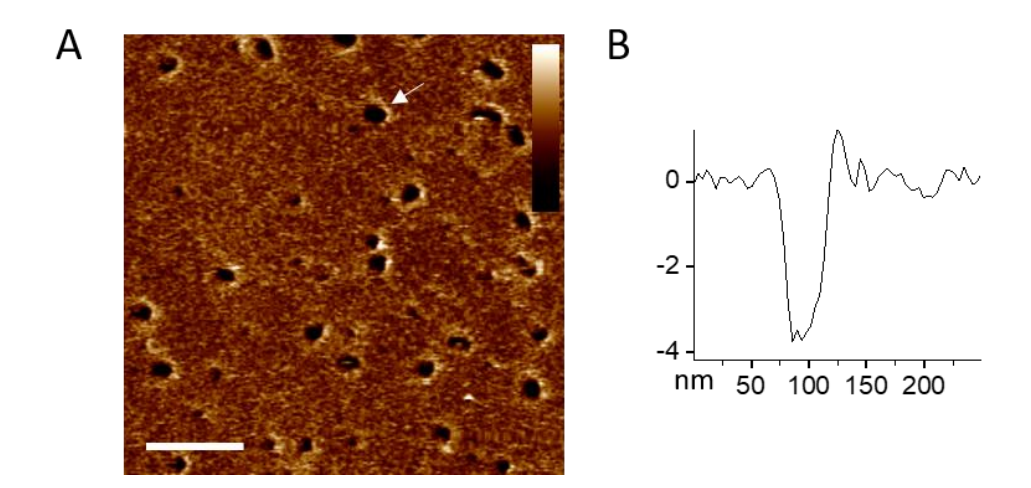


Figure S4. Membrane disruption with higher concentrations of magainin 2. AFM topography image of anionic POPC/POPG (3:1, molar ratio) SLB treated with magainin 2 (200 nM, 20 min incubation). Transmembrane pores with a heterogenous diameter of 5-40 nm form across the surface. Scale and colour bars are 200 nm and 5 nm, respectively.

**Video S1. Time-resolved scanning of membrane disruption by NI01.** The video shows consecutive scans from 3 min prior to peptide injection, to 30 min after peptide injection, for anionic POPC/POPG (3:1, molar ratio) SLBs treated with NI01 (375 nM). The video is recorded in a Cypher ES, with an AC10 cantilever, in tapping mode, at a line rate of 20 Hz and 25.8 seconds per frame. Scan size is 4 μm.

Video S2. Time-resolved scanning of membrane disruption at higher NI01 concentrations. The video shows consecutive scans from 1 min prior to peptide injection, to 6 min after peptide injection, for anionic POPC/POPG (3:1, molar ratio) SLBs treated with NI01 (750 nM). The video is recorded in a Cypher ES, with an AC10 cantilever, in tapping mode, at a line rate of 20 Hz and 23.8 seconds per frame. Scan size is 4  $\mu$ m.